AAS 19-364

SECOND-ORDER ANALYTICAL SOLUTION FOR RELATIVE MOTION ON ARBITRARILY ECCENTRIC ORBITS

Matthew Willis*, Alan Lovell†, and Simone D'Amico‡

A new, second-order solution for the relative position and velocity of two spacecraft on Keplerian orbits of arbitrary eccentricity is introduced. By normalizing the coordinates, changing the independent variable from time to true anomaly, and treating the higher-order terms as a perturbation of the resulting linear, time-varying system, the dynamics are rendered in a readily solvable form. A comparison of error trends against eccentricity and inter-spacecraft separation is presented between the new solution and several prominent translational state solutions from the literature. The new solution offers several orders of magnitude improvement in accuracy over existing first- and second-order solutions when evaluated against the underlying Keplerian motion model.

.

INTRODUCTION

The dynamics of spacecraft relative motion have been the subject of renewed interest as distributed space systems have come to be seen as a mission-enabling technology. Potential commercial and scientific applications for formation-flying spacecraft include on-orbit inspection and servicing, planetary topography and gravity recovery, as well as observations of gravitational waves and direct imaging of extrasolar planets.[1] Advanced formation guidance, navigation, and control algorithms are needed to make such missions a reality, and these will rely heavily on the model used to describe the dynamics of the system. Due to the limited processing power typical of satellite hardware, computational efficiency can be as important as the accuracy of a dynamics model for onboard implementation. Analytical solutions are particularly valuable because their accuracy is not tied to an integration step size or iteration tolerance, and therefore does not scale uniformly with computational cost.

Relative motion solutions may be broadly divided between those based on orbital elements and those using a translational state representation.[2] A thorough survey of existing dynamics models and solutions in both categories was conducted by Sullivan and D'Amico.[3] Orbital element representations are fundamentally connected to the underlying physics and relative motion geometry, thereby offering better accuracy and providing a natural framework for handling perturbations. These properties have been exploited by Koenig et al. to derive efficient state transition matrices for the most important forces affecting satellites in Earth orbit.[4] More recently, Kuiack and Ulrich built upon earlier work by Gurfil and others to develop a nonlinear orbital elements-based solution that includes J_2 perturbations.[5,6] However, translational state representations have advantages of

*PhD Candidate, Department of Mechanical Engineering, Stanford University, 496 Lomita Mall, Stanford, CA 94305.
†Space Vehicles Directorate, Air Force Research Laboratory, Kirtland, NM 87116.
‡Professor, Department of Aeronautics and Astronautics, Stanford University, 496 Lomita Mall, Stanford, CA 94305.

their own. Solutions based on the relative position and velocity are closely tied to the state observables and may be preferable for relative navigation applications. For that reason, the present work is focused on high-fidelity solutions in this category.

The best-known translational state solution is that of Clohessy and Wiltshire (CW), which addresses the linear, time-invariant problem of relative motion between two spacecraft in close proximity on near-circular orbits.[7] A second-order solution to the circular orbit problem was independently derived shortly after CW by London and Sasaki and later by Stringer and Newman.[8–10] This solution is frequently referred to as the Quadratic-Volterra (QV) solution in reference to the polynomial approximation technique upon which it is based.[11] For slightly elliptical orbits, the nonlinear effects are typically smaller than the effect of eccentricity. Melton introduced a linear, time-explicit solution that includes eccentricity as a perturbation to the circular-orbit dynamics.[12] More recent work by Butcher, et al. has extended Melton's solution into a family of second- and third-order solutions for the circular and slightly-eccentric cases.[13] Because these solutions are explicit in time, they avoid the need to numerically solve Kepler's equation for true anomaly at fixed times.[14]

The dynamics governing the temporal evolution of relative position and velocity on eccentric orbits are inherently nonlinear. However, Tschauner and Hempel (TH) provided a linear description of these dynamics by appropriately normalizing the coordinates and changing the independent variable from time to true anomaly.[15] Solutions to the TH equations introduced by Tschauner and Hempel, Carter, and others offered better accuracy than the CW solution in slightly eccentric orbits but suffered from singularities at zero eccentricity.[16] A nonsingular, linear solution to the problem of Keplerian relative motion on arbitrarily eccentric orbits was introduced by Yamanaka and Ankersen (YA).[17] Their major contribution was to base the solution on a new integral that grows in proportion to time. Figure 1 summarizes the interrelationship of the models discussed and their relevant domains in terms of spacecraft separation and orbit eccentricity. The present work completes the picture by introducing a second-order translational-state solution which is applicable to reference orbits of arbitrary eccentricity.

The remainder of this paper is divided into two parts, the first of which is the derivation of the new solution. For completeness, a development of the equations of relative motion to second order in inter-spacecraft separation and review of the YA solution are included. These are followed by a description of the solution procedure and presentation of the resulting equations. The second half of the paper demonstrates the accuracy of the solution through a series of example scenarios and

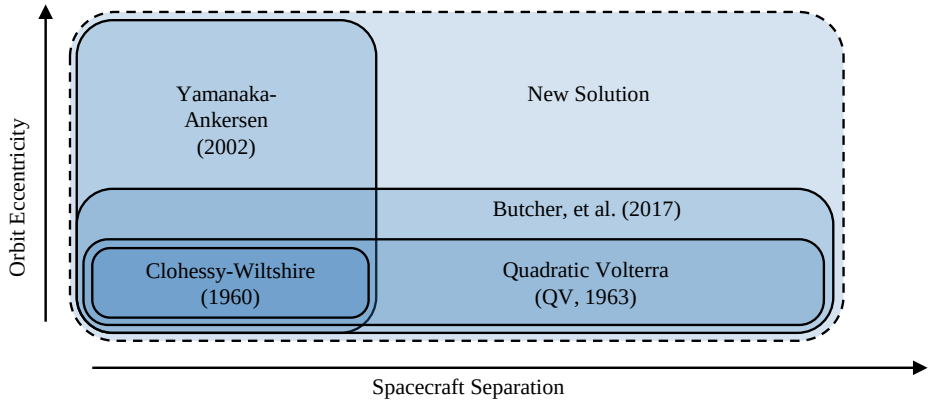

Figure 1. Illustrative Comparison of Translational State Solutions

compares its performance with the other translational state models included in Figure 1. The paper concludes with a brief summary of the results and discussion of future directions for research.

SOLUTION DERIVATION

Second-Order Equations of Motion

We express the motion of a deputy spacecraft relative to a chief spacecraft in terms of the position vector $\mathbf{r}$ from the central body to the chief and the relative position vector $\boldsymbol{\delta}\mathbf{r}$ from the chief to the deputy. Substituting these quantities into the fundamental orbital differential equation for the deputy spacecraft, we obtain

$$ {}^{I}\ddot{\mathbf{r}} + {}^{I}\ddot{\boldsymbol{\delta}\mathbf{r}} = -\mu \frac{\mathbf{r} + \boldsymbol{\delta}\mathbf{r}}{\|\mathbf{r} + \boldsymbol{\delta}\mathbf{r}\|^3} \tag{1} $$

where ${}^{I}(\dot{})$ indicates the time derivative with respect to an inertial frame. To isolate $\boldsymbol{\delta}\mathbf{r}$, we assume that $\delta r \ll r$ and expand $\|\mathbf{r} + \boldsymbol{\delta}\mathbf{r}\|^3$ using a binomial series. Truncating at second order in $(\delta r/r)$, the right-hand side of Equation (1) becomes

$$ -\mu \frac{\mathbf{r} + \boldsymbol{\delta}\mathbf{r}}{\|\mathbf{r} + \boldsymbol{\delta}\mathbf{r}\|^3} \approx -\frac{\mu}{r^3}\left(\mathbf{r} + \boldsymbol{\delta}\mathbf{r} - 3\frac{\mathbf{r}\cdot\boldsymbol{\delta}\mathbf{r}}{r^2}(\mathbf{r} + \boldsymbol{\delta}\mathbf{r}) - \frac{3}{2}\frac{\delta r^2}{r^2}\mathbf{r} + \frac{15}{2}\frac{(\mathbf{r}\cdot\boldsymbol{\delta}\mathbf{r})^2}{r^4}\mathbf{r}\right) \tag{2} $$

The first term in the series expansion is the acceleration ${}^{I}\ddot{\mathbf{r}}$ of the chief in the inertial frame and can be subtracted from both sides of Equation (1). We wish to express the relative motion in the Radial-Transverse-Normal (RTN) coordinate system rotating with the chief's orbit. Let ${}^{L}(\dot{})$ denote a time derivative with respect to this rotating frame, $\boldsymbol{\delta}\mathbf{v} \equiv {}^{L}\dot{\boldsymbol{\delta}\mathbf{r}}$ be the relative velocity, and $\boldsymbol{\omega}$ be the angular velocity of the rotating frame with respect to the inertial frame. Applying the theorem of Coriolis and using the fact that ${}^{I}\dot{\boldsymbol{\omega}} = {}^{L}\dot{\boldsymbol{\omega}} = \dot{\boldsymbol{\omega}}$, we obtain the equations of relative motion to second order in spacecraft separation,

$$ {}^{L}\ddot{\boldsymbol{\delta}\mathbf{r}} = -\frac{\mu}{r^3}\left(\boldsymbol{\delta}\mathbf{r} - 3\frac{\mathbf{r}\cdot\boldsymbol{\delta}\mathbf{r}}{r^2}(\mathbf{r} + \boldsymbol{\delta}\mathbf{r}) - \frac{3}{2}\frac{\delta r^2}{r^2}\mathbf{r} + \frac{15}{2}\frac{(\mathbf{r}\cdot\boldsymbol{\delta}\mathbf{r})^2}{r^4}\mathbf{r}\right) - 2\boldsymbol{\omega}\times\boldsymbol{\delta}\mathbf{v} - \dot{\boldsymbol{\omega}}\times\boldsymbol{\delta}\mathbf{r} - \boldsymbol{\omega}\times\boldsymbol{\omega}\times\boldsymbol{\delta}\mathbf{r} \tag{3} $$

Following the approach of Tschauner and Hempel, we change the independent variable from time to true anomaly f and normalize the coordinates by the chief's orbit radius. For convenience, we introduce the parameters

$$ k^2 = \sqrt{\frac{\mu}{p^3}} \tag{4} $$

$$ \rho = \frac{p}{r} = 1 + e\cos f \tag{5} $$

where $p = a(1 - e^2)$ is the semi-latus rectum. In the case of unperturbed Keplerian motion, $\omega = k^2\rho^2$. We will denote the normalized coordinates with $\tilde{(\,)}$ and derivatives with respect to true anomaly by $(\,)'$. The transformed relative position $\boldsymbol{\delta}\tilde{\mathbf{r}}$ and relative velocity $\boldsymbol{\delta}\tilde{\mathbf{v}} = {}^{L}\boldsymbol{\delta}\tilde{\mathbf{r}}'$ are related to $\boldsymbol{\delta}\mathbf{r}$ and $\boldsymbol{\delta}\mathbf{v}$ by

$$ \begin{aligned} \boldsymbol{\delta}\tilde{\mathbf{r}} &= \frac{1}{r}\boldsymbol{\delta}\mathbf{r} \\ \boldsymbol{\delta}\tilde{\mathbf{v}} &= -\frac{e}{p}\boldsymbol{\delta}\mathbf{r}\sin f + \frac{1}{k^2\rho p}\boldsymbol{\delta}\mathbf{v} \end{aligned} \tag{6} $$

$$\begin{aligned}\boldsymbol{\delta}\mathbf{r} &= r\,\boldsymbol{\delta}\tilde{\mathbf{r}} \\ \boldsymbol{\delta}\mathbf{v} &= k^2 p\,(e\boldsymbol{\delta}\tilde{\mathbf{r}}\sin f + \rho\boldsymbol{\delta}\tilde{\mathbf{v}})\end{aligned} \tag{7}$$

Expressing the relative position using its components in the chief's RTN coordinates as $\boldsymbol{\delta}\mathbf{r} = [x, y, z]^T$ and applying the necessary transformations leads to the explicit form of the second-order equations of relative motion,

$$\begin{aligned}\tilde{x}'' - 2\tilde{y}' - \frac{3}{\rho}\tilde{x} &= -\frac{3}{\rho}\tilde{x}^2 + \frac{3}{2\rho}(\tilde{y}^2 + \tilde{z}^2) \\ \tilde{y}'' + 2\tilde{x}' &= \frac{3}{\rho}\tilde{x}\tilde{y} \\ \tilde{z}'' + \tilde{z} &= \frac{3}{\rho}\tilde{x}\tilde{z}\end{aligned} \tag{8}$$

In Equation (8), the first-order terms that appear in the Tschauner-Hempel equations have been moved to the left while the nonlinear, second-order terms remain on the right-hand side. It is the effect of the latter terms that we wish to capture in the new solution.

Yamanaka-Ankersen Solution

Yamanaka and Ankersen found an analytical solution to the linear system of equations obtained by dropping the right-hand side of Equation (8),

$$\begin{aligned}\tilde{x}'' - 2\tilde{y}' - \frac{3}{\rho}\tilde{x} &= 0 \\ \tilde{y}'' + 2\tilde{x}' &= 0 \\ \tilde{z}'' + \tilde{z} &= 0\end{aligned} \tag{9}$$

The details of their derivation will be discussed in more detail in the context of the new solution in the following subsection. Their key contribution was to eliminate singularities in the solution to the TH equations by introducing the integral $J(t)$, defined as

$$J(t) = \int_{f_0}^{f} \frac{d\tau}{\rho(\tau)^2} = k^2(t - t_0) \tag{10}$$

Although the integration is taken over true anomaly, $J(t)$ is a linear function of time. The solution to Equation (9) is given by the linear system

$$\begin{bmatrix}\tilde{x} \\ \tilde{y} \\ \tilde{z} \\ \tilde{x}' \\ \tilde{y}' \\ \tilde{z}'\end{bmatrix} = \begin{bmatrix} \left(1 - \frac{3}{2}e\rho J(t)\sin f\right) & \rho\sin f & \rho\cos f & 0 & 0 & 0 \\ -\frac{3}{2}\rho^2 J(t) & (1+\rho)\cos f & -(1+\rho)\sin f & 1 & 0 & 0 \\ 0 & 0 & 0 & 0 & \sin f & \cos f \\ -\frac{3}{2}e\left((\rho\sin f)' J(t) + \frac{\sin f}{\rho}\right) & (\rho\sin f)' & (\rho\cos f)' & 0 & 0 & 0 \\ \frac{3}{2}(2e\rho J(t)\sin f - 1) & -2\rho\sin f & e - 2\rho\cos f & 0 & 0 & 0 \\ 0 & 0 & 0 & 0 & \cos f & -\sin f \end{bmatrix} \begin{bmatrix}K_1 \\ K_2 \\ K_3 \\ K_4 \\ K_5 \\ K_6\end{bmatrix} \tag{11}$$

where $(\rho\sin f)' = \cos f + e\cos 2f$ and $(\rho\cos f)' = -(\sin f + e\sin 2f)$, and K_1 through K_6 are integration constants. Note that the relative velocity components are computed by differentiation of the solution for the corresponding relative position component with respect to true anomaly. In the

limit as $e \to 0$, we may substitute $\rho \to 1$, $J(t) \to n(t - t_0)$, and $f \to n(t - t_{ref})$ to recover the CW equations rotated by the arbitrary reference angle nt_{ref}.

To express the solution in terms of initial conditions, one may solve for the integration constants by inverting Equation (11) and evaluating at the initial time t_0. Using $J(t_0) = 0$, this leads to

$$\begin{bmatrix} K_1 \\ K_2 \\ K_3 \\ K_4 \\ K_5 \\ K_6 \end{bmatrix} = \begin{bmatrix} \frac{6\rho_0+2e^2-2}{1-e^2} & 0 & 0 & \frac{2e\rho_0 \sin f_0}{1-e^2} & \frac{2\rho_0^2}{1-e^2} & 0 \\ -3\left(1+\frac{e^2}{\rho_0}\right)\frac{\sin f_0}{1-e^2} & 0 & 0 & \frac{\rho_0 \cos f_0 - 2e}{1-e^2} & -\frac{1+\rho_0}{1-e^2}\sin f_0 & 0 \\ -3\frac{e+\cos f_0}{1-e^2} & 0 & 0 & -\frac{\rho_0 \sin f_0}{1-e^2} & -\frac{e+(1+\rho_0)\cos f_0}{1-e^2} & 0 \\ -3e\left(1+\frac{1}{\rho_0}\right)\frac{\sin f_0}{1-e^2} & 1 & 0 & \frac{e\rho_0 \cos f_0 - 2}{1-e^2} & -e\frac{1+\rho_0}{1-e^2}\sin f_0 & 0 \\ 0 & 0 & \sin f_0 & 0 & 0 & \cos f_0 \\ 0 & 0 & \cos f_0 & 0 & 0 & -\sin f_0 \end{bmatrix} \begin{bmatrix} \tilde{x} \\ \tilde{y} \\ \tilde{z} \\ \tilde{x}' \\ \tilde{y}' \\ \tilde{z}' \end{bmatrix}_0 \tag{12}$$

The product of the matrices in Equations (11) and (12) is the famous YA state transition matrix for relative motion on eccentric orbits.

Second-Order Solution

Higher-order solutions to the equations of relative motion may be found by treating the true solution as a series expansion

$$\begin{aligned} \boldsymbol{\delta\tilde{\mathbf{r}}} &= \boldsymbol{\delta\tilde{\mathbf{r}}}_1 + \boldsymbol{\delta\tilde{\mathbf{r}}}_2 + \boldsymbol{\delta\tilde{\mathbf{r}}}_3 + \cdots \\ \begin{bmatrix} \tilde{x} \\ \tilde{y} \\ \tilde{z} \end{bmatrix} &= \begin{bmatrix} \tilde{x}_1 \\ \tilde{y}_1 \\ \tilde{z}_1 \end{bmatrix} + \begin{bmatrix} \tilde{x}_2 \\ \tilde{y}_2 \\ \tilde{z}_2 \end{bmatrix} + \begin{bmatrix} \tilde{x}_3 \\ \tilde{y}_3 \\ \tilde{z}_3 \end{bmatrix} + \cdots \end{aligned} \tag{13}$$

in which $\boldsymbol{\delta\tilde{\mathbf{r}}}_1 = [\tilde{x}_1, \tilde{y}_1, \tilde{z}_1]^T$ captures effects up to $O(\delta r/r)$, $\boldsymbol{\delta\tilde{\mathbf{r}}}_2 = [\tilde{x}_2, \tilde{y}_2, \tilde{z}_2]^T$ captures effects up to $O(\delta r^2/r^2)$, and so forth. The first-order solution $\boldsymbol{\delta\tilde{\mathbf{r}}}_1$ is precisely the YA solution in Equation (11). For convenience, the initial conditions of $\boldsymbol{\delta\tilde{\mathbf{r}}}_i$ and $\boldsymbol{\delta\tilde{\mathbf{v}}}_i$ are chosen to be zero for $i > 1$. The first-order solution is therefore exact at the initial state, i.e. $\boldsymbol{\delta\tilde{\mathbf{r}}}(f_0) \equiv \boldsymbol{\delta\tilde{\mathbf{r}}}_1(f_0)$, and the higher-order components account for the accumulation of error in the first-order solution. This assumption is beneficial because it allows us to use Equation (12) to define the integration constants K_1 through K_6 without having to invert a higher-order system.

To derive the second-order solution $\boldsymbol{\delta\tilde{\mathbf{r}}}_2$, we substitute Equation (13) into Equation (8) and expand the right-hand side. The only terms in the expansion that contribute to the $\boldsymbol{\delta\tilde{\mathbf{r}}}_2$ solution are those that are linear in $\boldsymbol{\delta\tilde{\mathbf{r}}}_2$ or quadratic in $\boldsymbol{\delta\tilde{\mathbf{r}}}_1$. Terms involving products of $\boldsymbol{\delta\tilde{\mathbf{r}}}_1$ and $\boldsymbol{\delta\tilde{\mathbf{r}}}_2$ components will contribute to $\boldsymbol{\delta\tilde{\mathbf{r}}}_3$ and terms quadratic in $\boldsymbol{\delta\tilde{\mathbf{r}}}_2$ will contribute to $\boldsymbol{\delta\tilde{\mathbf{r}}}_4$. Higher-order effects due to terms truncated in the derivation of Equation (8) from Equation (3) will be at least $O(\delta r^3/r^3)$ and have no contribution to $\boldsymbol{\delta\tilde{\mathbf{r}}}_2$. Thus, the second-order components solve the system formed by substituting the first-order solution into the nonlinear terms on the right-hand side of Equation (8),

$$\begin{aligned} \tilde{x}_2'' - \frac{3}{\rho}\tilde{x}_2 - 2\tilde{y}_2' &= -\frac{3}{\rho}\tilde{x}_1^2 + \frac{3}{2\rho}(\tilde{y}_1^2 + \tilde{z}_1^2) \\ \tilde{y}_2'' + 2\tilde{x}_2' &= \frac{3}{\rho}\tilde{x}_1\tilde{y}_1 \\ \tilde{z}_2'' + \tilde{z}_2 &= \frac{3}{\rho}\tilde{x}_1\tilde{z}_1 \end{aligned} \tag{14}$$

The system in Equation (14) simplifies the dynamics of Equation (8) by decoupling the out-of-plane component $\tilde{z}_2$ from the in-plane components $\tilde{x}_2$ and $\tilde{y}_2$. The in-plane equations can be decoupled by integrating the $\tilde{y}_2''$ equation once to obtain the system,

$$\begin{aligned} \tilde{x}_2'' - \frac{3}{\rho}\tilde{x}_2 - 2\tilde{y}_2' &= -\frac{3}{\rho}\tilde{x}_1^2 + \frac{3}{2\rho}(\tilde{y}_1^2 + \tilde{z}_1^2) \\ \tilde{y}_2' &= -2\tilde{x}_2 + 3\int \frac{\tilde{x}_1\tilde{y}_1}{\rho} df + c_{y1} \end{aligned} \tag{15}$$

where the constant of integration c_{y1} has been explicitly removed from the integral on the right-hand side. Applying the zero initial conditions to $\tilde{y}_2'$ and $\tilde{x}_2$, we find that $c_{y1} = -3\int(\tilde{x}_1\tilde{y}_1/\rho)df|_{f_0}$. Substituting the expression for $\tilde{y}_2'$ into the first equation leads to a second-order linear inhomogeneous ODE for $\tilde{x}_2$,

$$\tilde{x}_2'' + \left(4 - \frac{3}{\rho}\right)\tilde{x}_2 = -\frac{3}{\rho}\tilde{x}_1^2 + \frac{3}{2\rho}(\tilde{y}_1^2 + \tilde{z}_1^2) + 6\int \frac{\tilde{x}_1\tilde{y}_1}{\rho} df + 2c_{y1} \tag{16}$$

Second-order components of the relative motion appear only on the left of Equation (16), while the right may be written as an explicit function of f using Equation (11).

Equation (16) can be solved by variation of parameters if two linearly independent solutions are available for the homogeneous equation[18]

$$\tilde{x}_2'' + \left(4 - \frac{3}{\rho}\right)\tilde{x}_2 = 0 \tag{17}$$

Because the higher-order terms involving $\tilde{x}_1$ and $\tilde{y}_1$ do not appear in the homogeneous equation, it is identical to that obtained from the TH equations. The solutions to this equation introduced by Yamanaka and Ankersen are

$$\begin{aligned} \varphi_1 &= \rho\sin f \\ \varphi_2 &= 3e^2\rho J(t)\sin f + \rho\cos f - 2e \end{aligned} \tag{18}$$

and their linear independence was demonstrated in that work.[17] The particular solution φ_p to any inhomogeneous equation formed by placing an arbitrary function $RHS(f)$ of the independent variable on the right of Equation (17) can be found using the variation of parameters formula,

$$\varphi_p = \varphi_1\int \frac{\varphi_2 RHS(f)}{1-e^2} df - \varphi_2\int \frac{\varphi_1 RHS(f)}{1-e^2} df \tag{19}$$

where the denominator is $\varphi_1'\varphi_2 - \varphi_1\varphi_2' = 1 - e^2$. By superposition, the general solution is the sum of the particular solution and a linear combination of the homogeneous solutions φ_1 and φ_2:

$$\tilde{x}_2 = c_{x1}\varphi_1 + c_{x2}\varphi_2 + \varphi_p \tag{20}$$

We use Equations (11), (16), (18), (19), (20), and the zero initial conditions to solve for the second-order perturbation $\tilde{x}_2$ to the relative motion in the radial direction. The perturbation $\tilde{y}_2$ in the along-track direction is found by direct integration of the second line of Equation (15) using the solution for $\tilde{x}_2$ and zero initial conditions. Finally, applying the variation of parameters procedure to the third line of Equation (8) using the homogeneous solutions $\varphi_1 = \sin f$ and $\varphi_2 = \cos f$ and

$\varphi_1'\varphi_2 - \varphi_1\varphi_2' = 1$ results in the out-of-plane perturbation $\tilde{z}_2$. Combining these perturbations with the first-order components in Equation (11), we obtain the new analytical solution to the equations of relative motion accurate to second-order in $(\delta r/r)$,

$$
\begin{aligned}
\tilde{x} &= K_1\left(1-\frac{3}{2}e\rho J(t)\sin f\right) + K_2\rho\sin f + K_3\rho\cos f \\
&\quad + c_{xj}\left(1-\frac{3}{2}e\rho J(t)\sin f\right) + c_{xs}\rho\sin f + c_{xc}\rho\cos f - K_2K_4\cos f + K_3K_4\sin f \\
&\quad + \frac{1}{4}\left(K_1^2 - (K_2^2+K_3^2)(1+\rho) - 2K_4^2 - K_5^2 - K_6^2\right) \\
&\quad - \frac{9}{8}K_1^2\rho^3J(t)^2 + \frac{3}{2}(K_1K_2\cos f - K_1K_3\sin f + K_1K_4)\rho^2J(t) - K_5K_6\frac{2e\sin f + \sin 2f}{2(1-e^2)} \\
&\quad + \frac{1}{4}\left((1+\rho)(K_3^2-K_2^2) + K_5^2 - K_6^2\right)\cos 2f + K_2K_3\frac{(1+\rho)}{2}\sin 2f \\
\\
\tilde{y} &= K_4 + K_2(1+\rho)\cos f - K_3(1+\rho)\sin f - \frac{3}{2}K_1\rho^2J(t) \\
&\quad + c_{xs}\left((1+\rho)\cos f - (1+\rho_0)\cos f_0\right) - c_{xc}\left((1+\rho)\sin f - (1+\rho_0)\sin f_0\right) - \frac{3}{2}c_{xj}\rho^2J(t) \\
&\quad + \frac{3}{2}K_1K_2\rho J(t)\sin f + \frac{3}{2}K_1K_3(e+\cos f)\rho J(t) - \frac{3}{2}K_1K_4e\rho J(t)\sin f \\
&\quad + (K_3^2e - K_2K_4)(\sin f - \sin f_0) - \left(K_2K_3e + K_3K_4 + K_5K_6\frac{2e}{1-e^2}\right)(\cos f - \cos f_0) \\
&\quad - \frac{1}{2}\left(K_2K_3 + \frac{K_5K_6}{1-e^2}\right)(\cos 2f - \cos 2f_0) + \frac{1}{4}(K_3^2 - K_2^2 + K_6^2 - K_5^2)(\sin 2f - \sin 2f_0) \\
\\
\tilde{z} &= K_5\sin f + K_6\cos f \\
&\quad + \left((K_3K_6 - K_2K_5)\sin^3 f_0 - 3K_3K_6\sin f_0 + (K_2K_6 + K_3K_5)\cos^3 f_0\right)\sin f \\
&\quad + \left((K_2K_5 - K_3K_6)\cos^3 f_0 - 3K_2K_5\cos f_0 + (K_2K_6 + K_3K_5)\sin^3 f_0\right)\cos f \\
&\quad + \frac{3}{2\rho_0}\left(K_1K_5(e+\cos f_0) - K_1K_6\sin f_0\right)\sin(f - f_0) \\
&\quad + \frac{3}{2}(K_2K_5 + K_3K_6) - \frac{3}{2}K_1K_5\rho J(t)(e+\cos f) + \frac{3}{2}K_1K_6\rho J(t)\sin f \\
&\quad + \frac{1}{2}(K_2K_5 - K_3K_6)\cos 2f - \frac{1}{2}(K_2K_6 + K_3K_5)\sin 2f
\end{aligned}
\tag{21}
$$

where the constants c_{xj}, c_{xs}, and c_{xc} are expressed in the appendix as functions of the integration constants K_1 through K_6 and the initial true anomaly. As with the YA solution, the integration constants are found from the initial conditions using Equation (12) while Equations (6) and (7) are used to convert to and from the transformed coordinates, respectively.

Several features of Equation (21) deserve special attention. First, neglecting all terms involving products of the integration constants will return the YA solution. This fact is obvious by construction but emphasizes that the new solution is an extension of the YA solution in the same sense that QV is an extension of CW. Next, consider the limit as $e \to 0$. Making the substitutions $\rho \to 1$,

$J(t) \to n(t-t_0)$, $f \to n(t-t_{ref})$, and $f_0 \to n(t_0-t_{ref})$ and setting $t_0 = t_{ref} = 0$, Equation (21) becomes

$$
\begin{aligned}
x &= K_1 + K_2 \sin t + K_3 \cos t \\
&\quad + \frac{3}{4}\left(-K_1^2 - 2K_3^2 + 2(K_2+K_4)(3K_2+K_4) + K_5^2 + K_6^2\right) - 3K_1K_3 \\
&\quad - \left(2K_2K_3 - K_5K_6 + \frac{3}{2}K_1(K_2+K_4)\right)\sin t \\
&\quad + \left(\frac{3}{4}K_1^2 + K_3^2 - \left(4K_2^2 + 6K_2K_4 + \frac{3}{2}K_4^2 + K_5^2 + \frac{1}{2}K_6^2\right) + 3K_1K_3\right)\cos t \\
&\quad + \frac{3}{2}K_1K_4 t - \frac{9}{8}K_1^2 t^2 + \frac{3}{2}K_1K_2 t\cos t - \frac{3}{2}K_1K_3 t \sin t \\
&\quad + \frac{1}{4}\left(-2K_2^2 + 2K_3^2 + K_5^2 - K_6^2\right)\cos 2t + \left(K_2K_3 - \frac{1}{2}K_5K_6\right)\sin 2t \\
\\
y &= K_4 + 2K_2\cos t - 2K_3 \sin t - \frac{3}{2}K_1 t \\
&\quad + \frac{3}{2}\left(3K_2K_3 + 2K_3K_4 + 2K_1(K_2+K_4) - K_5K_6\right) \\
&\quad - \left(4K_2K_3 + 3K_3K_4 + 3K_1(K_2+K_4) - 2K_5K_6\right)\cos t \\
&\quad + \left(-\frac{3}{2}K_1^2 + 8K_2^2 - 2K_3(3K_1+K_3) + 9K_2K_4 + 3K_4^2 + 2K_5^2 + K_6^2\right)\sin t \\
&\quad + \frac{3}{2}\left(K_1^2 + 3K_1K_3 - 5K_2^2 + K_3^2 - 6K_2K_4 - 2K_4^2 - K_5^2 - K_6^2\right)t + \frac{3}{2}K_1K_3 t\cos t + \frac{3}{2}K_1K_2 t \sin t \\
&\quad - \frac{1}{2}(K_2K_3 + K_5K_6)\cos 2t - \frac{1}{4}(K_2^2 - K_3^2 + K_5^2 - K_6^2)\sin 2t \\
\\
z &= K_5 \sin t + K_6 \cos t \\
&\quad + \left(K_3K_5 + K_2K_6 + \frac{3}{2}K_1K_5\right)\sin t - (2K_2K_5 + K_3K_6)\cos t \\
&\quad + \frac{3}{2}(K_2K_5 + K_3K_6) - \frac{3}{2}K_1K_5 t\cos t + \frac{3}{2}K_1K_6 t \sin t \\
&\quad + \frac{1}{2}(K_2K_5 - K_3K_6)\cos 2t - \frac{1}{2}(K_3K_5 + K_2K_6)\sin 2t
\end{aligned}
\tag{22}
$$

which is identical to the QV solution. The choices of t_0 and t_{ref} are arbitrary given the symmetry of the circular orbit. Setting them to zero only serves to simplify the equations when written as functions of the integration constants. Neglecting the second-order terms in this form leaves the CW equations intact, completing the relationships between the new solution and the YA, QV, and CW solutions shown in Figure 1.

PERFORMANCE COMPARISON

Having completed the derivation of the second-order solution, we wish to demonstrate its accuracy and compare its performance with other solutions in the literature. These models are evaluated

against an unperturbed Keplerian truth to show how well each captures the relative motion subject to the assumptions under which it was derived. This choice reduces the number of parameters needed to fully specify the chief's absolute motion to three: semimajor axis, eccentricity, and true anomaly. Combined with the six parameters needed to characterize the relative motion, we have a nine-dimensional state space. Rather than attempting a full parameter sweep, we compare performance in three test scenarios and highlight essential trends.

Validation Scenarios

The three test scenarios are chosen to illuminate the effects of chief orbit eccentricity and inter-spacecraft separation. First we examine a scenario in the near-circular regime, then consider moderate and high eccentricity scenarios. To maintain consistency and feasibility, all scenarios are initialized at perigee with an altitude h_p of 750 km. This causes the semimajor axes to be larger for the more eccentric cases, so these scenarios must be simulated over a longer time T_{sim} to allow for multiple orbits. Table 1 summarizes the absolute orbit parameters for the three scenarios.

Several equivalent representations can be used to specify the relative motion. We will use the quasi-nonsingular relative orbit elements (ROE), which are defined in terms of the Keplerian orbital elements of the chief and deputy as

$$\begin{bmatrix} \delta a \\ \delta\lambda \\ \delta e_x \\ \delta e_y \\ \delta i_x \\ \delta i_y \end{bmatrix} = \begin{bmatrix} \frac{a_d - a_c}{a_c} \\ (u_d - u_c) + (\Omega_d - \Omega_c)\cos i_c \\ e_d \cos\omega_d - e_c \cos\omega_c \\ e_d \sin\omega_d - e_c \sin\omega_c \\ i_d - i_c \\ (\Omega_d - \Omega_c)\sin i_c \end{bmatrix} \tag{23}$$

where $u = M + \omega$ is the mean argument of latitude. Unlike the components of relative position and velocity, all of the ROE are constant for unperturbed orbital motion except $\delta\lambda$. For near-circular orbits, the extent of the relative motion in the radial direction is proportional to the L_2-norm of the relative eccentricity vector $\boldsymbol{\delta e} = [\delta e_x, \delta e_y]^T$ and the extent of the out-of-plane motion is proportional to the L_2-norm of the relative inclination vector $\boldsymbol{\delta i} = [\delta i_x, \delta i_y]^T$. The mean along-track separation is given by $a_c\delta\lambda$ and along-track drift is governed by $a_c\delta a$.

Table 2 summarizes the initial ROE selected for the three scenarios. Each includes a 100 m difference in semimajor axis to introduce an along-track drift. The relative eccentricity and inclination vectors are chosen in scenario 1 to ensure passive collision avoidance as the deputy drifts with respect to the chief. In scenarios 1 and 3, there is a moderately large initial separation in the along-track direction. Scenario 2 eliminates this initial offset and increases the extent of the relative orbit by a factor of five. For all simulations, the initial conditions in Tables 1 and 2 are converted to orbital elements and Earth-centered inertial coordinates for the chief and deputy. These are then

Table 1. Chief Orbit Parameters and Duration for Performance Comparison Scenarios

Scenario	h_p (km)	e_c	i_c	Ω_c	ω_c	f_0	T_{sim} (hr)
1	750	0.001	98°	30°	30°	0°	4
2	750	0.1	98°	30°	30°	0°	5
3	750	0.8	98°	30°	30°	0°	40

Table 2. Initial ROE for Performance Comparison Scenarios

Scenario	$a_c\delta a$ (km)	$a_c\delta\lambda$ (km)	$a_c\delta e_x$ (km)	$a_c\delta e_y$ (km)	$a_c\delta i_x$ (km)	$a_c\delta i_y$ (km)
1	0.1	5	0	0.5	0	0.5
2	0.1	0	0	2.5	0	2.5
3	0.1	5	0	0.5	0	0.5

used to compute the RTN components of relative position $\boldsymbol{\delta r_{RTN}} = [x, y, z]^T$ and relative velocity $\boldsymbol{\delta v_{RTN}} = [\dot{x}, \dot{y}, \dot{z}]^T$ that can be input to the various relative motion solutions. The truth model performs the transformation from orbital elements to relative position and velocity at each time step, solving Kepler's equation to find the true anomaly.

Figure 2 shows the trajectories produced for scenario 1 by the Keplerian truth, new solution, and a selection of solutions from the literature. These include CW, YA, QV, and six solutions that treat the chief's eccentricity as a perturbation to the circular orbit dynamics. The latter are characterized by the parameter q that represents the perturbing strength of eccentricity relative to inter-spacecraft separation, as well as the maximum order in separation of eccentricity terms included in the solution. For $q = 1$, the $O(\varepsilon^{1/q})$ solution includes terms up to $e_c x$ and x^2 and is therefore second order in separation. For $q = 2$, $O(\varepsilon^{4/q})$, the highest-order terms are of the form $e_c^2 x$, $e_c x^2$, and x^3, so the solution is third order in separation. In the figure, all solutions are style- and color-coded according to their order and underlying assumptions, respectively. Dashed lines indicate a linear model, dash-dot a second-order model, and dotted a third-order model. Blue lines are used for models that assume circular orbits, red fully incorporate eccentricity through coordinate transformation, and green, yellow, and violet treat eccentricity as an increasingly significant perturbation to the circular orbit dynamics. The light blue line representing CW indicates that the solution in spherical coordinates is being used to account for the along-track separation.

Under the innocuous conditions of scenario 1, all models are accurate to within the resolution of Figure 2 except for YA. For that model, the use of rectilinear coordinates results in poor handling of radial separation and an incorrect along-track drift. Errors in the other models are better visualized in Figure 3, which plots the L_2-norm of the relative position error vectors over time. Because all solutions are initialized with the exact relative position and velocity, all errors rise quickly from zero to a nearly constant magnitude. After YA, the CW and QV solutions give the largest errors. The performance of these solutions is nearly identical because the second-order rectilinear terms in QV effectively capture the same dynamics accounted for by the use of the spherical CW solution. In this near-circular case, the second-order perturbation solutions perform only slightly worse than the new solution which fully incorporates eccentricity effects. The best performance is achieved by the third-order solutions which most accurately handle the effects of inter-spacecraft separation. Just as QV obscures CW in the figure, the lines corresponding to the second- and third-order $q = 2$ solution are obscured by the corresponding $q = 3$ lines.

Figures 4 and 5 show the relative trajectories and position errors for scenario 2. Due to the much larger eccentricity $e_c = 0.1$, the models that assume a circular chief orbit completely fail to describe the relative motion. Those that assume small eccentricity also lead to very significant errors. Despite the large increase in separation, the YA solution's performance is comparable to that of scenario 1 because there is no initial along-track offset. The same is true for its second-order counterpart, which maintains sub-meter accuracy. This is an order of magnitude better than the best

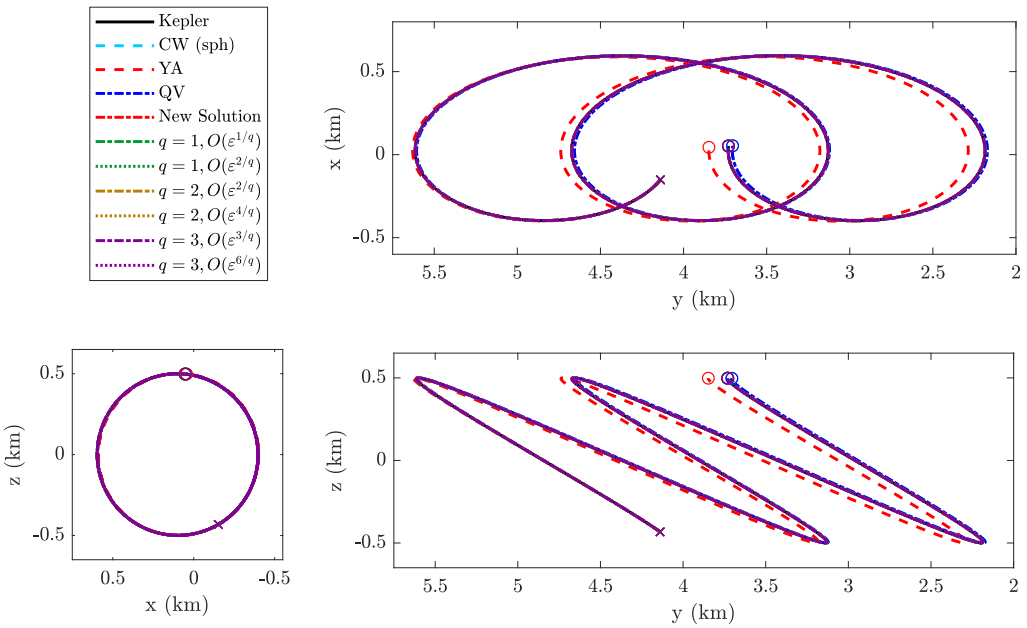

Figure 2. Trajectory Comparison for Scenario 1

performance achieved by any of the third-order solutions for scenario 2 and far better still than the second-order solutions that treat eccentricity as a perturbation.

The last scenario tests performance in a highly eccentric orbit. The solutions evaluated on this scenario in Figures 6 and 7 are restricted to YA, its second-order extension, and the third-order solution which performed best of the perturbing-eccentricity solutions in the previous scenarios. With $e_c = 0.8$ it is no longer appropriate to treat eccentricity effects as a mere perturbation of the circular orbit dynamics, and the third-order solution leads to the very large errors shown in Figure 7. Its trajectory prediction is excluded from Figure 6 for clarity. The linear YA solution produces similarly unacceptable errors although it does a slightly better job of capturing the general behavior. On the other hand, our new second-order solution traces the truth model trajectory very

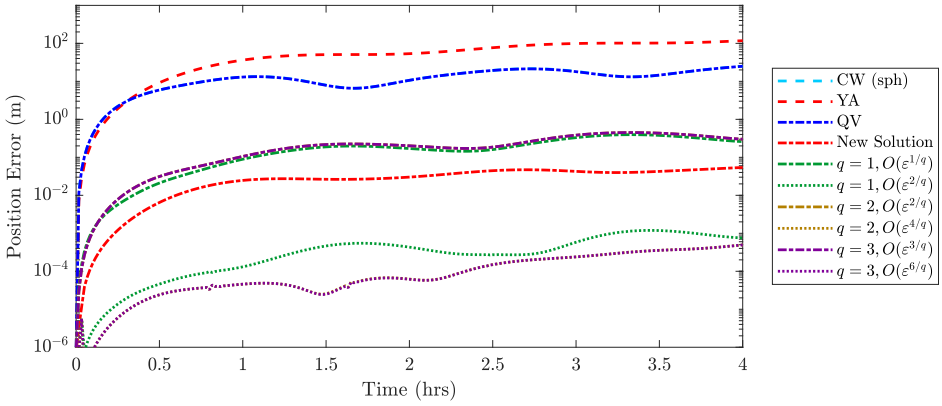

Figure 3. Relative Position Error Comparison for Scenario 1

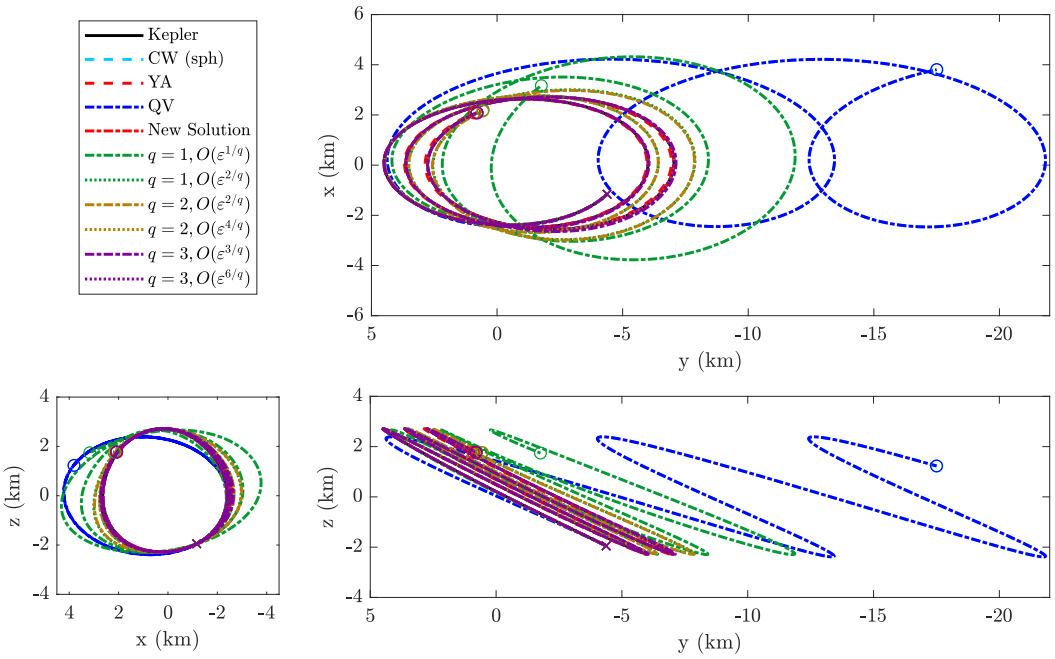

Figure 4. Trajectory Comparison for Scenario 2

well. As Figure 7 clarifies, its accuracy stays near the meter level throughout most of the simulation. Large error spikes occur near perigee where high relative acceleration magnifies any error present.

One of the primary motivators for analytical solutions is reducing the computational burden for onboard implementation. To evaluate on that objective, Table 3 lists the wall-clock runtimes for each of the solutions tested in scenarios 1 and 2. All calculations were performed in MATLAB on a system equipped with an Intel Core i7 two-core 2.70 GHz processor. The times are averaged over the number of evaluations in the simulated scenarios with 1 s intervals. For the truth model, YA solution, and new eccentric solution, this includes the time spent solving Kepler's equation to find the true anomaly. Calculations were streamlined for each solution by evaluating a minimal set of trigonometric functions and using identities to compute more complicated expressions from their

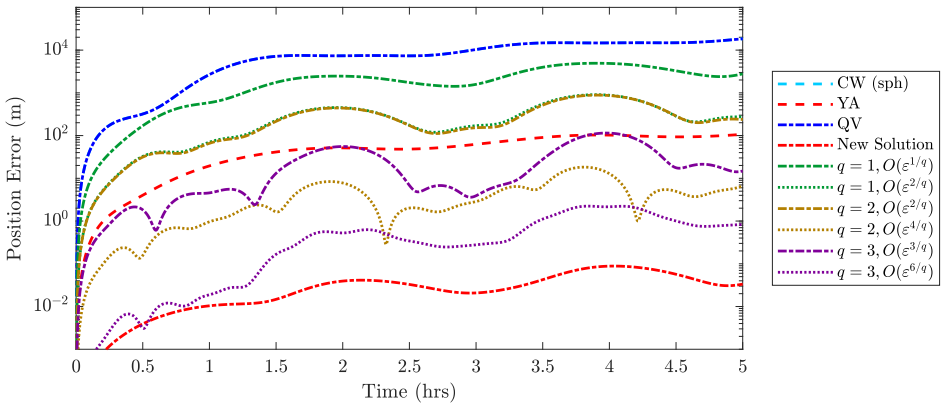

Figure 5. Relative Position Error Comparison for Scenario 2

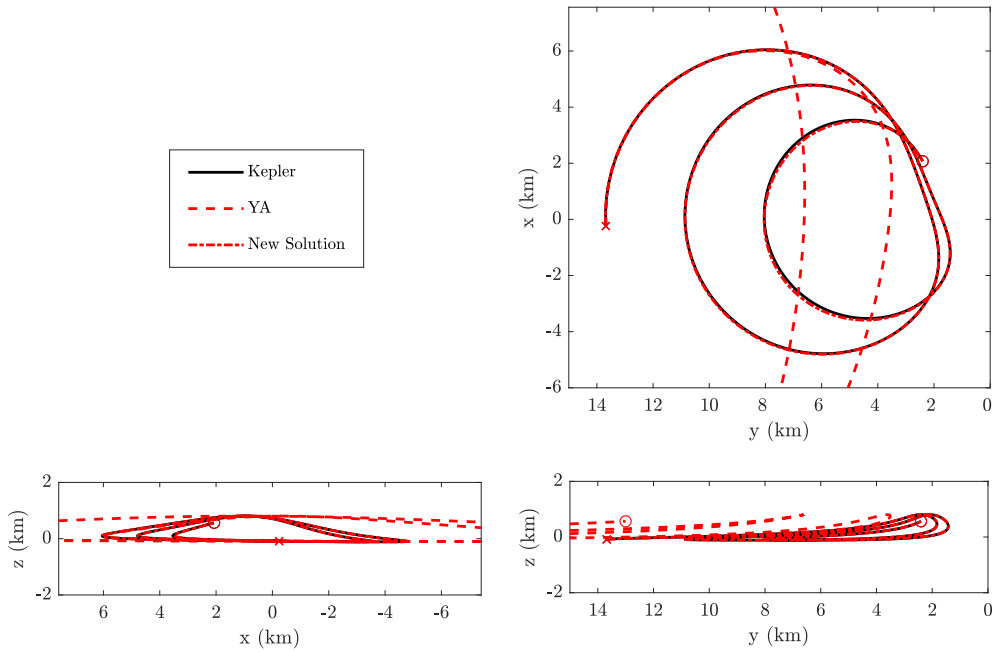

Figure 6. Trajectory Comparison for Scenario 3

stored values. This reduced the number of trigonometric function evaluations by three orders of magnitude for the $q = 3, O(\varepsilon^{6/q})$ solution.

The CW and QV solutions for circular orbits are the fastest because they require the fewest trigonometric function evaluations. Despite being linear, YA is slightly more expensive than CW because it includes the time required to solve Kepler's equation. Although their second-order extensions appear far more complicated on paper, the computational cost increases by less than a third when going from CW to QV or YA to the new solution. In the latter case, this is a small price to pay for the enormous improvement in accuracy demonstrated in Figures 3, 5, and 7. Solutions that treat the eccentricity as a perturbation of the circular orbit dynamics can be very computationally expen-

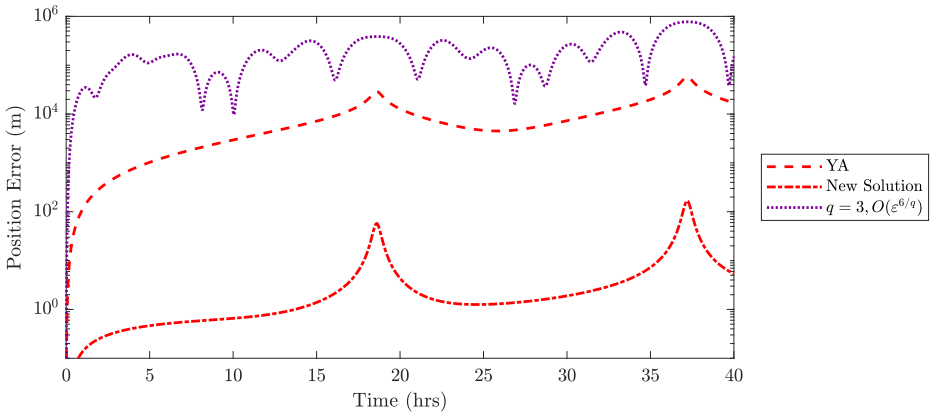

Figure 7. Relative Position Error Comparison for Scenario 3

Table 3. Runtime comparison for several relative motion models

Solution	Runtime (μs)	Percent of Keplerian Truth
Keplerian Truth	71	100
CW	0.53	0.75
YA	0.92	1.3
QV	0.59	0.84
New Solution	1.2	1.6
$q = 1, O(\varepsilon^{1/q})$	0.65	0.92
$q = 1, O(\varepsilon^{2/q})$	11	15
$q = 2, O(\varepsilon^{2/q})$	0.73	1.0
$q = 2, O(\varepsilon^{4/q})$	15	21
$q = 3, O(\varepsilon^{3/q})$	1.8	2.6
$q = 3, O(\varepsilon^{6/q})$	22	31

sive despite being time-explicit. It is important to note that runtime depends on implementation as well as processing power. Care was taken to ensure that all solutions were implemented consistently, but the more complicated solutions might be accelerated through algebraic manipulation.

Broad Trends

The previous section emphasized the error behavior in time for a few concrete examples. We will now explore broader error trends across the models studied. Because our new solution generalizes earlier second-order solutions to arbitrarily eccentric orbits, we are especially interested in how each solution's error changes when we increase e_c from 0 to 1.

Figure 8 compares the maximum error over 10 orbits of ten relative motion solutions against the eccentricity of the chief's orbit. All simulations are initialized at perigee with an altitude of 750 km and have initial ROE $a_c[\delta a, \delta\lambda, \delta e_x, \delta e_y, \delta i_x, \delta i_y]^T = [0, 0, 0, 2, 0, 2]^T$ km. Because there is no initial along-track offset, the Cartesian CW solution is used instead of its spherical counterpart. As suggested by the test scenarios in the last section, the third-order perturbation solutions are the most accurate at very low eccentricities, but their performance degrades as e_c increases. The YA and new solution are much less sensitive until the eccentricity is very high. In particular, the new second-order solution gives errors several orders of magnitude better than all other solutions for e_c between 0.1 and 0.9. The presence of $1 - e_c^2$ in the denominator of several terms in Equations (12) and (21) makes these solutions singular for parabolic orbits and causes the error to diverge near $e_c = 1$.

The semi-log representation of Figure 8 highlights the accuracy improvement of the new solution, but it masks a wealth of interesting behavior at small eccentricities. To reveal this region, we present the same data on a log-log plot in Figure 9. In this format it is clear how the solutions stratify by order in the circular orbit limit. The two linear solutions, CW and YA, give the highest error in this extreme. The second-order solutions give a very large improvement in accuracy, more than three orders of magnitude in the scenario shown. Further extending the solution to third order gives a somewhat smaller improvement.

As eccentricity increases, the second-order solutions differentiate according to how strongly they treat its effects on the dynamics. QV begins to lose accuracy around $e_c = 10^{-5}$ and the perturbation

solutions around $e_c = 10^{-4}$. Similar differentiation occurs between CW and YA near $e_c = 10^{-3}$, the classical boundary of the near-circular orbit regime, and among the third-order perturbation solutions from 10^{-3} to 10^{-2}. The YA solution and its second-order extension do not begin to lose accuracy until the eccentricity is greater than 10^{-1}. As the effects of eccentricity come to dominate

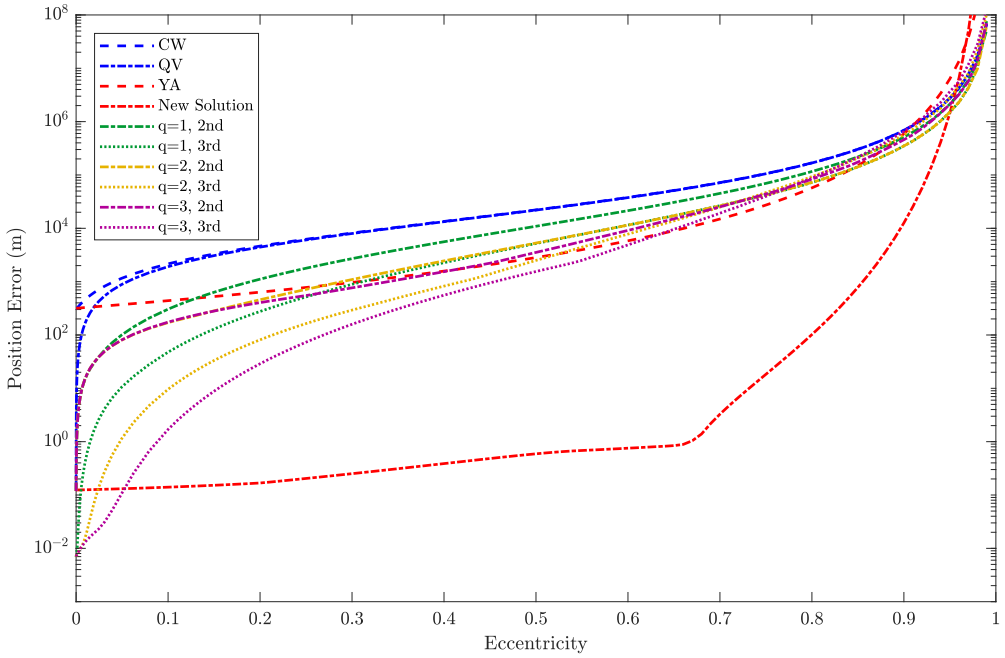

Figure 8. Maximum Position Error Against Eccentricity

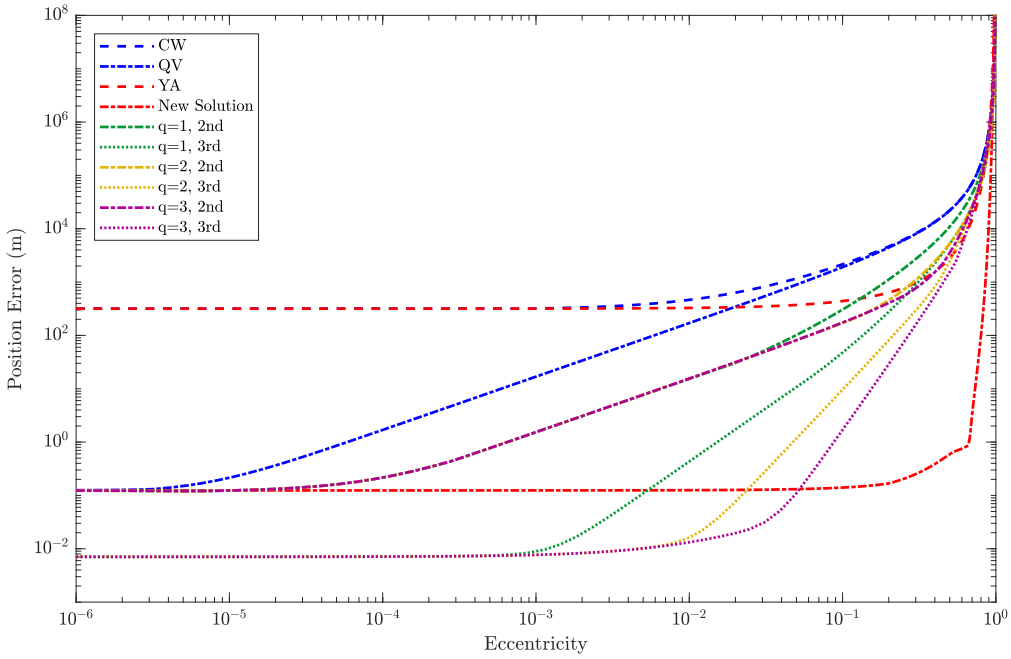

Figure 9. Maximum Position Error Against Eccentricity on a Logarithmic Scale.

the effects of inter-spacecraft separation, the QV solution converges with CW and the second-order $q = 2$ solution converges with the third-order $q = 1$ solution.

The performance of the solutions against increasing separation is as important as that against eccentricity. Figure 10 compares the maximum position error of the same set of translational state solutions against a Keplerian truth model over 10 orbits as a function of separation. The simulations initialize the chief's orbit using the conditions for scenario 1 in Table 1 and the relative motion using $a_c[\delta a, \delta\lambda, \delta e_x, \delta e_y, \delta i_x, \delta i_y]^T = \delta r_{ref}[0, 0, 0, 1, 0, 1]^T$. For this comparison, δr_{ref} ranges from 10 cm to 1000 km. The position error shown is normalized by δr_{ref} to provide a relative error and clarify the scaling. Thus, a horizontal line represents a constant proportionality between separation and error or a linear error growth. The noisy boundary in the bottom-left corner of the plot is the result of numerical error at the micrometer level.

At large separations, the solutions group by their order. However, the solutions do not group by their underlying assumptions at small separations the way they do for large eccentricity in Figure 9. The most interesting information on display in Figure 10 is provided by the slopes of the lines, which indicate the terms that are driving the error. The CW and YA solutions converge to a line with unit slope on this log-log plot, indicating quadratic error growth. As the separation decreases, the solutions differentiate according to their underlying assumptions. At small separations, the CW and QV solutions are virtually identical and limited by the near-circular orbit assumption. Their accuracy is then driven by the leading, first-order terms and they converge to a constant proportionality between separation and error. The linear YA solution fully accounts for eccentricity effects, so its error scales quadratically over the full range of separation. Similarly, the error line for the new solution has a slope of two for separations less than 10 km, indicating that the truncated third-order

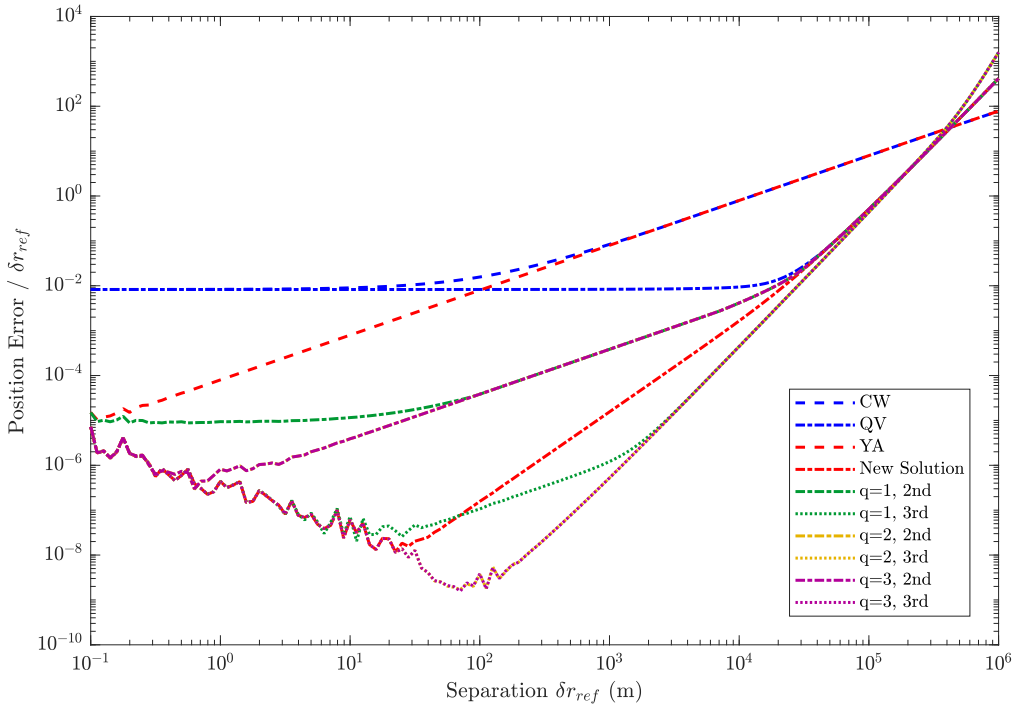

Figure 10. Maximum Position Error Against Separation for $e_c = 0.001$

terms drive the error. The second-order solutions that treat eccentricity as a perturbation break away from the new solution around this same threshold. Their errors are dominated by approximations in the quadratic terms at intermediate separations and linear terms at the smallest separations. A similar pattern is followed by the third-order solutions. For separations less than 100 km, the slope of three indicates that the truncated fourth-order terms dominate. Errors in the $q = 2$ and $q = 3$ solutions follow this slope beyond the numerical precision limit, while error in the $q = 1$ solution is dominated by the approximation in the second-order terms for separation less than 1 km.

In the near-circular scenario used to generate Figure 10, many of the higher-order solutions reach the numerical precision threshold with little differentiation. Figure 11 further illuminates the behavior by exploring the case when the chief eccentricity is increased to $e_c = 0.1$. All other simulation conditions are identical to those of the previous figure. The increase in eccentricity causes the solutions that treat eccentricity as a perturbation to stratify by q value. It is clear that there is some separation for each of these solutions below which its error is dominated by the linear terms and another below which it is dominated by the quadratic terms. On the other hand, the behavior of the new and YA solutions is virtually unchanged from Figure 10 because they are insensitive to eccentricity below $e_c \approx 0.2$ (cf. Figure 9). Not only is the new solution the most accurate for separations below 20 km in this scenario, but its improvement over other translational state solutions increases as the separation decreases. This makes it particularly well-suited for missions involving a wide range of operating distances.

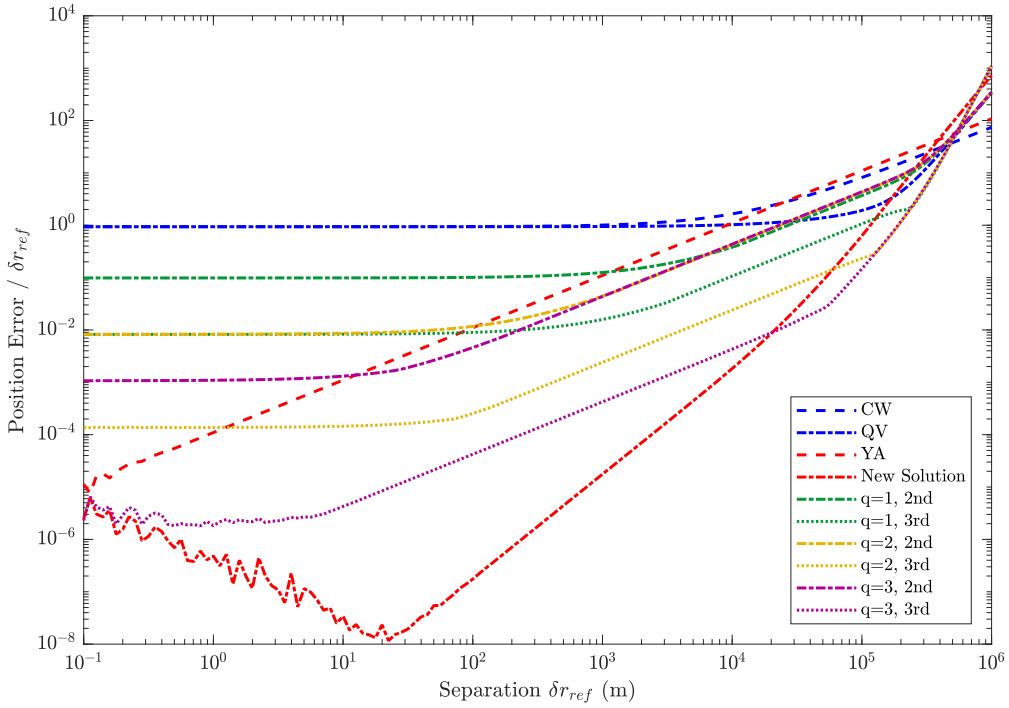

Figure 11. Maximum Position Error Against Separation for $e_c = 0.1$

Comparison with ROE model

Up to this point we have exclusively considered translational state solutions that are closely related to the new solution presented in this work. However, many authors favor solutions based on

orbital elements, either through orbit element differences or the ROE defined in Equation (23). Because the orbital elements are constants of motion in the two-body problem, they map to relative position and velocity with zero error compared to a Keplerian truth. For control system design in the orbital element state space, it is preferable to approximate the dynamics so that the solution is linear in the state variables. In the case of ROE, this affects only the mean relative argument of latitude $\delta\lambda$ because each of the other ROE are constant with respect to Keplerian dynamics. Expanding the nonlinear terms to second order, $\delta\lambda$ is given by

$$\delta\lambda \approx \delta\lambda_0 - \frac{3}{2} n_c \, t\delta a + \frac{15}{8} n_c \frac{t}{a_c} \, \delta a^2 \tag{24}$$

where n_c is the mean motion of the chief spacecraft.

Figure 12 compares the performance of YA and the new solution with that obtained by propagating the ROE using the approximate model in Equation (24) for scenario 2. Solutions for $\delta\lambda$ truncated at first and second order in δa are included and the exact nonlinear mapping from ROE to relative position and velocity is used. Recall from Figure 5 that the new solution was the most accurate of the translational state solutions for scenario 2. Figure 12 reveals that even the simplest, first-order approximation of the ROE evolution results in comparably small position errors and even smaller relative velocity errors. Extending the approximation to second order further suppresses these errors by several orders of magnitude to a level near the numerical precision of the simulation.

The ROE representation is extremely useful for guidance and control applications because it describes the relative motion efficiently and accurately. However, this representation introduces a computational trade-off when state observables such as relative position must be dealt with. While

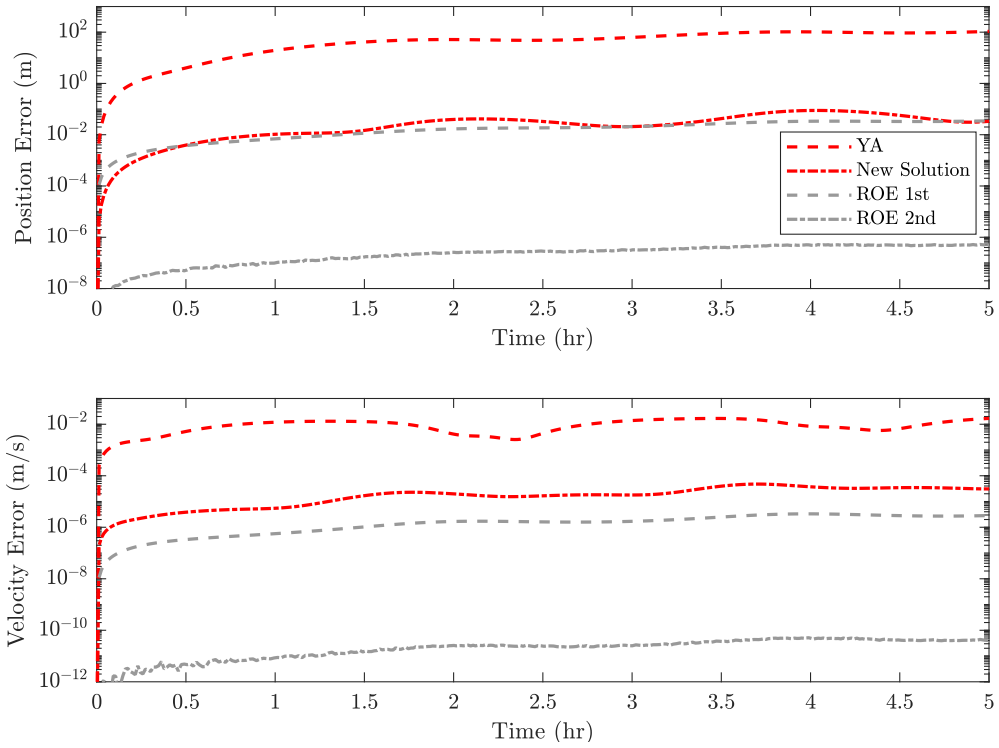

Figure 12. Relative Position and Velocity Error Comparison for Scenario 2

the propagation of the ROE state in time is extremely fast, the transformation from ROE to relative position and velocity is the same as that used by the Keplerian truth model throughout this analysis. Thus, Table 3 provides a sense of the computational cost of the ROE solution compared to the other solutions when translational state variables must be known.

CONCLUSION

This paper introduced a new, second-order solution for the relative motion of two spacecraft in arbitrarily eccentric orbits. The derivation extended the linear Yamanaka-Ankersen solution using the same scheme previously used to derive the Quadratic Volterra solution from that of Clohessy and Wiltshire. By treating the second-order effects as a perturbation to the first-order result, the nonlinear differential equation is reduced to a linear inhomogeneous equation that is readily solvable for the higher-order terms. The new solution was validated against an unperturbed Keplerian truth model and compared with a variety of related solutions from the literature. Although third-order solutions that treat eccentricity as a perturbation are able to achieve higher accuracy at small eccentricities, they do so at great computational expense. By fully incorporating the effects of eccentricity on the dynamics through coordinate transformation, the new solution retains its accuracy up to very high eccentricity.

A useful application of the new solution would be initial relative orbit determination with angles-only navigation. This problem has a range ambiguity for linear systems that can be resolved with the inclusion of nonlinear features. Through its unification of existing translational state solutions, high accuracy across a broad range of orbit eccentricities and spacecraft separations, and relevance to current work in relative navigation, the solution introduced herein represents a major contribution to the state of the art in modeling spacecraft relative motion. However, the current form of the solution does not account for the presence of perturbations such as Earth oblateness, solar radiation pressure, and tidal effects from the sun and moon. Such perturbations will reduce the accuracy of the model and may obscure the effects of the higher-order terms. In addition to applying the new solution to the problem of relative orbit determination, future work should seek to incorporate leading order effects of other perturbations.

ACKNOWLEDGMENTS

This work was supported by the NASA Office of the Chief Technologist's Space Technology Research Fellowship, NASA grant number 80NSSC18K1176. The authors would also like to thank Eric Butcher and Ethan Burnett for providing the code for their higher-order solutions.

REFERENCES

[1] S. D'Amico, M. Pavone, S. Saraf, A. Alhussien, T. Al-Saud, S. Buchman, R. Bryer, and C. Farhat, "Distributed Space Systems for Future Science and Exploration," 8th International Workshop on Spacecraft Formation Flying, Delft University, June 8-10, 2015.

[2] K. T. Alfriend, S. R. Vadali, P. Gurfil, J. P. How, and L. S. Breger, *Spacecraft Formation Flying: Dynamics, control and navigation*. Elsevier, 2010.

[3] J. Sullivan, S. Grimberg, and S. D'Amico, "Comprehensive Survey and Assessment of Spacecraft Relative Motion Dynamics Models," *Journal of Guidance, Control, and Dynamics*, Vol. 40, No. 8, 2017, pp. 1837–1859.

[4] A. W. Koenig, T. Guffanti, and S. D'Amico, "New State Transition Matrices for Relative Motion of Spacecraft Formations in Perturbed Orbits," AIAA/AAS Astrodynamics Specialist Conference, Long Beach, CA, September 13-16, 2016.

[5] B. Kuiack and S. Ulrich, "Nonlinear Analytical Equations of Relative Motion on J2-Perturbed Eccentric Orbits," *Journal of Guidance, Control, and Dynamics*, Vol. 41, No. 12, 2018, pp. 2664–2675.

[6] P. Gurfil and K. V. Kholshevnikov, "Manifolds and Metrics in the Relative Spacecraft Motion Problem," *Journal of Guidance, Control, and Dynamics*, Vol. 29, No. 4, 2006, pp. 1004–1010.

[7] W. H. Clohessy and R. S. Wiltshire, "Terminal Guidance System for Satellite Rendezvous," *Journal of Guidance, Control, and Dynamics*, Vol. 27, No. 9, 1960, pp. 653–658.

[8] H. S. London, "Second Approximation to the Solution of the Rendezvous Equations," *AIAA Journal*, Vol. 1, No. 7, 1963, pp. 1691–1693.

[9] M. L. Anthony and F. T. Sasaki, "Rendezvous Problem for Nearly Circular Orbits," *AIAA Journal*, Vol. 3, No. 7, 1965, pp. 1666–1673.

[10] M. T. Stringer, B. A. Newman, T. A. Lovell, and A. Omran, "Analysis of a New Nonlinear Solution of Relative Orbital Motion," 23rd International Symposium on Space Flight DYnamics, Pasadena, California, October 29-November 2 2012.

[11] B. A. Newman, A. J. Sinclair, T. A. Lovell, and A. Perez, "Comparison of Nonlinear Analytical Solutions for Relative Orbital Motion," AIAA/AAS Astrodynamics Specialist Conference, San Diego, California, August 4-7 2014.

[12] R. G. Melton, "Time-Explicit Representation of Relative Motion Between Elliptical Orbits," *Journal of Guidance, Control, and Dynamics*, Vol. 23, No. 4, 2000, pp. 604–610.

[13] E. A. Butcher, E. Burnett, and T. A. Lovell, "Comparison of Relative Orbital Motion Perturbation Solutions in Cartesian and Spherical Coordinates," 27th AAS/AIAA Space Flight Mechanics Meeting, San Antonio, Texas, February 5-9, 2017.

[14] D. A. Vallado, *Fundamentals of Astrodynamics and Applications*. Springer, 2007.

[15] J. Tschauner and P. Hempel, "Optimale Beschleunigungsprogramme fur das Rendezvous-Manover," *Astronautica Acta*, Vol. 10, No. 5-6, 1964, p. 296.

[16] T. E. Carter, "State Transition Matrices for Terminal Rendezvous Studies: Brief Survey and New Example," *Journal of Guidance, Control, and Dynamics*, Vol. 21, No. 1, 1998, pp. 148–155.

[17] K. Yamanaka and F. Ankersen, "New State Transition Matrix for Relative Motion on an Arbitrary Elliptical Orbit," *Journal of Guidance, Control, and Dynamics*, Vol. 25, No. 1, 2002, pp. 60–66.

[18] W. E. Boyce and R. C. DiPrima, *Elementary Differential Equations*. Wiley, 2008.

APPENDIX: SOLUTION COEFFICIENTS

$$c_{xc} = \sum_i \sum_{k \geq i} c_{xcik} \tag{25}$$

$$c_{xc11} = \frac{3}{4} K_1^2 \frac{e + \cos f_0}{1 - e^2}$$

$$c_{xc12} = \frac{3}{2} K_1 K_2 \frac{e + (1 + \rho_0 + \rho_0^2) \cos f_0}{(1 - e^2)\rho_0} \sin f_0$$

$$c_{xc13} = \frac{3}{2} K_1 K_3 \frac{-2 + e^2 + \rho_0 + (1 + \rho_0 + \rho_0^2) \cos^2 f_0}{(1 - e^2)\rho_0}$$

$$c_{xc14} = \frac{3}{2} K_1 K_4 \frac{\sin f_0}{\rho_0}$$

$$c_{xc22} = K_2^2 \frac{e + 6 \cos f_0 - (5 + 3\rho_0(2 + \rho_0)) \cos^3 f_0}{2(1 - e^2)}$$

$$c_{xc23} = K_2 K_3 \frac{e^2 + 2(-3 + \rho_0 + \rho_0^2) + (5 + 3\rho_0(2 + \rho_0)) \cos^2 f_0}{1 - e^2} \sin f_0$$

$$c_{xc24} = K_2 K_4 \frac{4 - 3\rho_0 - (4 + 2\rho_0) \cos^2 f_0}{1 - e^2}$$

$$c_{xc33} = K_3^2 \frac{-6e - 12 \cos f_0 + ((2 + e^2) + 3(1 + \rho_0)^2) \cos^3 f_0}{2(1 - e^2)}$$

$$c_{xc34} = 2 K_3 K_4 \frac{2e + (2 + \rho_0) \cos f_0}{1 - e^2} \sin f_0$$

$$c_{xc44} = -\frac{3}{2} K_4^2 \frac{e + \cos f_0}{1 - e^2}$$

$$c_{xc55} = -K_5^2 \frac{2(e + \cos f_0) + \cos f_0 \sin^2 f_0}{2(1 - e^2)}$$

$$c_{xc56} = K_5 K_6 \frac{\sin^3 f_0}{1 - e^2}$$

$$c_{xc66} = -K_6^2 \frac{e + \cos^3 f_0}{2(1 - e^2)}$$

$$c_{xs} = \sum_i \sum_{k \geq i} c_{xsik} \tag{26}$$

$$c_{xs11} = \frac{3}{4} K_1^2 \frac{e^2 + \rho_0}{(1-e^2)\rho_0} \sin f_0$$

$$c_{xs12} = \frac{3}{4} K_1 K_2 \frac{1 + 3(\rho_0 - 1)\rho_0 - (1 + \rho_0 + \rho_0^2)\cos 2f_0}{(1-e^2)\rho_0}$$

$$c_{xs13} = \frac{3}{2} K_1 K_3 \frac{e - e\rho_0 + (1 + \rho_0 + \rho_0^2)\cos f_0}{(1-e^2)\rho_0} \sin f_0$$

$$c_{xs14} = -\frac{3}{2} K_1 K_4 \frac{e - e\rho_0 + \cos f_0}{(1-e^2)\rho_0}$$

$$c_{xs22} = -K_2^2 \frac{3 - 2\rho_0 - 3\rho_0^3 + \rho_0(5 + 3\rho_0(2 + \rho_0))\cos^2 f_0}{2(1-e^2)\rho_0} \sin f_0$$

$$c_{xs23} = K_2 K_3 \frac{e(\rho_0 - 3) - \cos f_0 (3 - \rho_0(7 + 4\rho_0(1 + \rho_0)) + \rho_0(5 + 3\rho_0(2 + \rho_0))\cos^2 f_0)}{(1-e^2)\rho_0}$$

$$c_{xs24} = -K_2 K_4 \frac{e\left(1 - \frac{3}{\rho_0}\right) + (4 + 2\rho_0)\cos f_0}{1 - e^2} \sin f_0$$

$$c_{xs33} = -K_3^2 \frac{6\rho_0(1 + \rho_0) - (3 + \rho_0)(1 - e^2) - (2(1 - e^2) + 3(1 + \rho_0)^2)\rho_0 \cos^2 f_0}{2(1-e^2)\rho_0} \sin f_0$$

$$c_{xs34} = K_3 K_4 \left(2 \frac{4 - (2 + \rho_0)\cos^2 f_0}{1 - e^2} - \frac{3}{\rho_0} \right)$$

$$c_{xs44} = -\frac{3}{2} K_4^2 \frac{\rho_0 + e^2}{(1-e^2)\rho_0} \sin f_0$$

$$c_{xs55} = K_5^2 \left(\frac{3}{2\rho_0} - \frac{7 - \cos 2f_0}{4(1-e^2)} \right) \sin f_0$$

$$c_{xs56} = K_5 K_6 \frac{3(e + \cos f_0) - (2 + \sin^2 f_0)\rho_0 \cos f_0}{(1-e^2)\rho_0}$$

$$c_{xs66} = -K_6^2 \frac{3 - \rho_0 \sin^2 f_0}{2(1-e^2)\rho_0} \sin f_0$$

$$c_{xj} = \sum_i \sum_{k \geq i} c_{xjik} \tag{27}$$

$$
\begin{aligned}
c_{xj11} &= K_1^2 \frac{1 - e^2 - 3\rho_0}{2(1 - e^2)} \\
c_{xj12} &= -3K_1 K_2 \frac{\rho_0^2}{1 - e^2} \sin f_0 \\
c_{xj13} &= -K_1 K_3 \frac{3\rho_0^2}{1 - e^2} \cos f_0 \\
c_{xj14} &= 0 \\
c_{xj22} &= K_2^2 \frac{1 - 2\rho_0^3 + (\rho_0 - 1 + 3\rho_0^2(1 + \rho_0)) \cos^2 f_0}{1 - e^2} \\
c_{xj23} &= 2K_2 K_3 \frac{e + \cos f_0 - (1 + 3\rho_0(1 + \rho_0))\rho_0 \cos f_0}{1 - e^2} \sin f_0 \\
c_{xj24} &= 2K_2 K_4 \frac{(\rho_0(1 + 2\rho_0) + e \cos f_0) \cos f_0 - e}{1 - e^2} \\
c_{xj33} &= K_3^2 \frac{5\rho_0^2 + (e + \cos f_0)^2 - (1 - e^2 + 3\rho_0(1 + \rho_0))\rho_0 \cos^2 f_0}{1 - e^2} \\
c_{xj34} &= -2K_3 K_4 \left(\frac{2\rho_0(1 + \rho_0)}{1 - e^2} - 1 \right) \sin f_0 \\
c_{xj44} &= K_4^2 \left(\frac{3\rho_0}{1 - e^2} - 1 \right) \\
c_{xj55} &= K_5^2 \frac{2(1 + e^2) + (\rho_0 - 1)(5 - \cos 2f_0)}{2(1 - e^2)} \\
c_{xj56} &= -K_5 K_6 \frac{2e \sin^3 f_0}{1 - e^2} \\
c_{xj66} &= K_6^2 \frac{1 + (\rho_0 - 1) \cos^2 f_0}{1 - e^2}
\end{aligned}
$$